Approaching the radiating X-point in SOLPS-ITER modeling of ASDEX Upgrade H-mode discharges

I.Yu.Senichenkov[1], E.G.Kaveeva[1], V.A.Rozhansky[1], S.P.Voskoboynikov[1], I.Yu.Veselova[1], N.V.Shtyrkhunov[1], D.P.Coster[2], X.Bonnin[3] and the ASDEX Upgrade Team.

[1] Peter the Great St.Petersburg Polytechnic University, 195251, Polytechnicheskaya ul., 29, Saint Petersburg, Russia

[2] Max-Planck Institut für Plasmaphysik, EURATOM Association, D-85748 Garching, Germany

[3] ITER Organization, 13067 St. Paul-lez-Durance, France

Abstract. In the present paper the ASDEX Upgrade (AUG) experimental trend of reaching the radiative X-point with nitrogen seeding is reproduced by SOLPS-ITER code modeling. In these experiments the whole divertor region below the X-point is cooled down by the impurity radiation if the seeding rate is large enough, and the maximal radiation is registered from the X-point region, or even from the confinement zone above the X-point.

It is demonstrated that for constant seeding rate SOLPS-ITER simulations of the intensively seeded AUG discharges result in that the confined plasma goes into the radiation collapse as a certain threshold in seeding rate is exceeded. This threshold value increases with increasing discharge power. No stable regimes with the electron temperature below 5 eV in the confinement zone even above the X-point are achieved in the modeling if the seeding rate is large enough, in contrast to experiment. However, such a regime may be achieved if the fueling, seeding and pumping rates are changing in time. Since the SOLPS-ITER code can simulate only steady state, another modeling strategy is chosen. The fueling and seeding rates are artificially reduced by 3 orders of magnitude and the impurity content are set to satisfy the condition that the ratio of electrons contribution originating from fuel atoms to ones coming from impurity atoms is about unity.

It is suggested that the radial width of the cooled region in the confinement zone is of the order of the SOL width λ_q, since it is driven by the same physics leading the energy flux to go from mostly radial to mostly parallel. Under these conditions, the radiative spot above the X-point behaves as the energy sink similarly to the energy sink near the divertor in the conventional regime. In extreme regimes (with large seeding rate), the width of the cold region inside the separatrix may exceed λ_q, and up to 90% of discharge power can be radiated from the confined region. An estimate of the poloidal length of the radiative spot is suggested as well.

Flow patterns of neutrals, deuterium ions, impurities, electric current and heat flows are analyzed for the regimes with intensive X-point radiation. The formation of an electric potential peak above the X-point is observed in the simulations, and the corresponding $E \times B$ drift flux appears to give the largest contribution to the main ion and impurity fluxes. This $E \times B$ drift flux together with the large ionization source change the parallel velocity with respect to its neoclassical profile. Consequently, the radial E field deviates from the neoclassical one, which might improve the turbulence suppression.

Keywords: plasma edge, SOL, impurity seeding, radiative X-point, detachment, electric field, drift, transport codes, SOLPS-ITER

PACS numbers: 52.55.Fa, 52.65.Kj

Submitted to: *Plasma Phys. Control. Fusion*

1. Introduction

Our current understanding of divertor physics indicates that at least partial detachment will be a necessary condition for operation of future fusion power devices such as ITER [1, 2, 3] and/or tokamaks of next generation (DEMO [4, 5], CFETR [6]), since it is the only regime which allows meeting the engineering requirements on the maximal heat flux density to the divertor targets. The operation in detached (or semi-detached) regime is proposed to be achieved by intensive impurity seeding into the divertor region in order to radiate up to 90% of the power coming from upstream [4].

The transition to detachment with intensive impurity seeding has been studied experimentally for many years, varying experimental conditions and the impurity gas species (N, Ne, Ar, or even Kr) [7, 8, 9, 10, 11, 12, 13, 14, 15, 16, 17, 18]. As for ASDEX Upgrade, the most success is achieved with N seeding, Ne is found to be not suitable [19], and experiments with Ar are currently underway [20]. The rough estimates of the amount of impurity required to reach full detachment at the outer divertor target is that the number of electrons provided by the impurity is approximately the same as the number of electrons provided by the fuel (deuterium). If this condition is satisfied, the possibility to control in real time the so-called degree of detachment and the degree of confinement reduction in the core is demonstrated via a feed-back loop controlling the impurity seeding rate.

On ASDEX Upgrade. with further increase of the impurity seeding rate, after the outer target fully detaches, the tokamak plasma moves to a new regime, which is characterized by the presence of a radiative spot in the confinement region above the X-point [9, 12, 14]. From tomography reconstructions, the size of the spot is estimated to be of the order of several cm, the radiated power density reaches the value of $25 - 30$ MW/m^3, and the estimated electron temperature is believed to be below 5 eV. The electron temperature obtained from the Balmer line ratio measurements is found to be even below 1 eV [9], which indicates the presence of intensive volume recombination.

On Alcator C-mod the radiating spot in the X-point vicinity was observed with N_2 seeding rather than with Ne or Ar [7], like in ASDEX Upgrade. In those experiments with intensive nitrogen seeding a significant reduction of energy flux to the outer divertor was registered as compared to the attached conditions, and it was explained by the irradiation of 85% of discharge power.

However, no dramatic reduction of the pedestal profiles is observed with the presence of the radiating spot above the X-point both on ASDEX Upgrade and on Alcator C-mod. And again, on ASDEX Upgrade the location of the spot and its vertical motion for up to about 10 cm above the X-point may be controlled in real time by adjusting the impurity seeding rate and the discharge power [21]. The most reliable observations of such a regime were achieved on ASDEX Upgrade with nitrogen seeding [9, 21, 22], and then were repeated on JET with both nitrogen [12] and neon [14]. This regime might be associated with the X-point MARFE [23, 24] and in some sense is similar to it, however, we will not use this term, following the suggestion and reasoning introduced in [19]: in contrast to MARFE, the newly observed regime does not lead to the unstable plasma. Note, however, that in DIII-D experiments no observations of the radiating X-point regime is reported, while the increase of nitrogen seeding leads to confinement degradation or even to radiation collapse of the discharge [22, 25].

The radiated power inside the separatrix might exceed 3/4 of the total discharge power, and therefore regimes with radiating spot above the X-point seem to be suitable for machines like DEMO. For 2 GW thermonuclear power, the power crossing the separatrix is 400 MW, while only 100 MW are estimated to be compatible with stable DEMO divertor operation [5]. An option to reduce this power is midplane Xe injection, and regimes with radiating X-point may be a possible alternative.

Anyway, such a regime opens new physics which is not yet understood. Attempts to reproduce

such a regime in 2D edge transport codes cannot be treated as fully successful. The simulation by SOLPS5.0 without drifts [26] results in reproducing the cold spot above the X-point, however, obtained solutions are reported to be marginally stable and prone to radiation collapse. Later it was demonstrated [27, 28] that full inclusion of drifts and currents changes the solution significantly, and that the inclusion of drifts in the model is essential. The importance of drifts is confirmed in the present paper. In both papers [27, 28], only a modest value of discharge power is considered - 5 MW, and no attempts are made to reproduce the radiating spot above the X-point. The reason for this is in fact that, in those simulations, increasing the seeding rate above a certain threshold leads to a radiation collapse.

In the present paper the question is raised whether the radiation collapse may be avoided by increasing the discharge power in the modeling. To do this, the series of SOLPS-ITER [29, 30] runs presented in [28] is supplemented with several additional cases, where the discharge power and nitrogen seeding rate are increased. We consider the single-null topology with the ion ∇B-induced drift directed downwards towards the X-point. This modeling series results in the conclusion that the radiation collapse is unavoidable in the modeling with the present version of the SOLPS-ITER code and with the applied boundary conditions. With increasing power the threshold value of the nitrogen seeding rate which still allows for stable solution increases, but if this threshold value is exceeded the modeling case goes into radiation collapse. For the maximal considered discharge power this threshold value is found to be about $1.2 \cdot 10^{21}$ nitrogen atoms per second, which remains about three times smaller than the experimental seeding rates.

After this finding was confirmed, we considered another series of modeling cases. In this new series, particle content is prescribed rather than fueling and/or seeding rate, using an alternative set of boundary conditions. Cases in this series differ from each other by nitrogen content, thus the feedback is modeled. The temperature at the core boundary is prescribed rather than discharge power, so the power adjusts to the radiation losses from impurities. In this second series the radiating spot above the X-point is well reproduced, and stable solutions are obtained for different power and nitrogen content.

This modeling series is analyzed in detail in the present paper. It is demonstrated that the temperature indeed falls down to the 1 eV range above the X-point, and this leads to a reduction of the electric conductivity. Thus a strong electric field is required to drive the parallel Pfirsch-Schlüter current — the mechanism is similar to one suggested in [31, 32, 33] — and a peak in electric potential appears. The resulting strong $E \times B$ drift gives the major contribution to both main ion and impurity fluxes. This drift flux together with the intensive ionization source significantly changes the parallel velocity with respect to its neoclassical profile, and leads to a significant deviation of the electric field from its neoclassical value. As a result, the shear of electric field gets stronger and this might lead to better turbulence suppression due to the presence of the cold zone above the X-point.

Analysis of heat flow in the outermost flux surfaces, affected by the radiating spot, shows that the situation is similar to the near scrape-off layer (SOL) in the conventional high-recycling regime: the radiating zone above the X-point behaves like a heat sink and in this sense is analogous to the heat sink in the divertor. The radial heat flux, which is maximal at the outer midplane, turns into a poloidal heat flux, and the power it transported is then radiated away at the bottom of the flux surface. Therefore, the characteristic radial width of the cross-field heat flux decay should be of the order of λ_q — the heat flux decay length in the near SOL. When the temperature drops to the value corresponding to maximal radiation, the poloidal energy flow ends, and from this condition it is possible to estimate the poloidal size of the radiating spot.

The rest of the paper is organized as following. In Section 2, the SOLPS-ITER code and the

model of ASDEX Upgrade discharge are described, partially repeating the corresponding section of the paper [28]. In Section 3, the modeling results for the series with prescribed discharge power, fueling and seeding rates are presented. The reason why this series appears to be unsuccessful are discussed, and the alternative modeling strategy is suggested. The results of the second modeling series are presented in Section 4, where the appearance of the radiating cold spot is demonstrated. Finally, the features of the observed regime are discussed in Section 5, where special attention is paid to the density and temperature distributions, particle and heat flow directions, electric currents and potential, and the role of drifts. Estimates of the radial and poloidal size of the radiating spot are suggested as well.

2. Modeling setup

The modeling cases presented here and below are based on ASDEX Upgrade shot #28903, where an H-mode deuterium plasma was seeded with nitrogen. The details of the experimental setup are described in [26, 27] and will not be considered further below, since no explicit comparison to the experimental data is assumed here.

Since the modeling cases considered here are in some sense the continuation of the series analyzed in [28], we also refer to that earlier work for the details of the modeling setup. Here we will concentrate on the difference between the series of runs from [28] and the cases analyzed here.

To perform the modeling, the SOLPS-ITER suite of codes is used. The main plasma solver is the 2-dimensional fluid code B2.5 [34] for plasma species, which is coupled to the Monte-Carlo core Eirene [35, 36] for neutral atoms and molecules (which are not affected by the magnetic field), and is supplemented by tools for the preprocessing, postprocessing and analysis of the results [30]. The computational domain for the B2.5 code and its computational representation together with its curvilinear coordinates are presented in Figure 1.

In all cases presented here, $E \times B$ drifts, diamagnetic drifts, and currents are fully turned on.

We start from the series of cases with 5 MW power crossing the separatrix with nitrogen seeding, analyzed in [28]. The very first aim is to investigate why does the modeling solution goes into radiation collapse with increasing nitrogen seeding rate and to try to overcome the difficulties which prevented obtaining a stable solution with the experimentally measured seeding rate for this discharge.

To do this, several attempts were made: turning off the speed-up scheme of the artificial poloidal averaging, turning on the flux-limiting coefficients for condctive heat fluxes in the confined region, adjusting the mesh resolution near the X-point and even changing the numerical treatment of drift terms. Details may be found in Appendix A.

Note that all this effort leads to a possibility to increase the maximum seeding rate value for the 5 MW discharge power series from $2 \cdot 10^{20}$ at/s (see [28]) to $3 \cdot 10^{20}$ at/s, however, this did not change the overall picture, see the detailed description in the next Section.

Finally, we expected that the increase of discharge power would help to

Another way considered to obtain a solution with the radiating spot above the X-point is to increase the discharge power. It has been expected (quite naturally) that the radiation collapse happens due to the lack of incoming power, so that with increasing discharge power it might be possible to avoid the radiation collapse keeping the nitrogen seeding rate at the experimental level. To verify this, the series of runs presented in the paper [**?**] for 5 MW of incoming power is partially repeated for 8, 12 and 15 MW correspondingly. The results are presented in the next section.

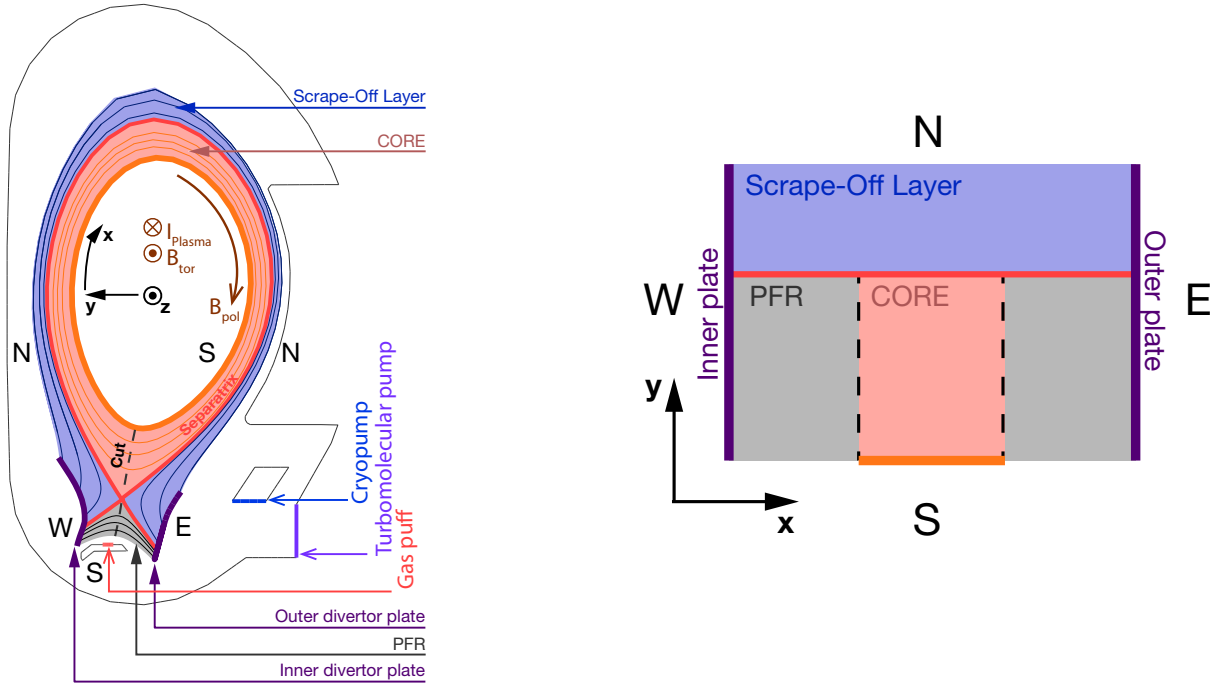

Figure 1. SOLPS-ITER computational mesh in physical space and the so-called computational representation of the B2.5 domain. Shown are directions of B-field components and plasma current, directions of curvilinear coordinates x, y and z, the location of divertor plates, location of gas puff and pumps. The location of different zones (CORE, Scrape-Off Layer – SOL, Private Flux Region – PFR) is shown on both the 'physical' and 'computational' meshes. Letters 'W', 'N', 'E', 'S' stand for 'western', 'northern', 'eastern' and 'southern' sides of the computational mesh.

3. High seeding rate cases

The cases considered here are summarized in Table 1. They all are similar to the nitrogen series presented in [28], the two only varying parameters are the nitrogen seeding rate and discharge power.

Let's start with a brief analysis of the impurity distribution for the series with fixed seeding rate and increasing discharge power. From Figure 2 one can see that the outer target regime varies from pronounced detachment at the smallest power to the sheath-limited regime at the highest power. The corresponding Z_{eff} profiles at the outer midplane (OMP) and the nitrogen enrichment along the flux surface located at 2 mm radially outward from the separatrix (as measured at the OMP) are plotted in Figure 3. These figures confirm the statement given in [28] that the closer the outer divertor is to detachment, the better the nitrogen is compressed near the outer target. From Figure 4

	P=5 MW	P=8 MW	P=12 MW	P=15 MW
$\dot{N} = 2 \cdot 10^{19}$ at/s	converged	converged	converged	converged
$\dot{N} = 2 \cdot 10^{20}$ at/s	converged	converged	converged	converged
$\dot{N} = 3 \cdot 10^{20}$ at/s	converged			
$\dot{N} = 5 \cdot 10^{20}$ at/s	rad. collapse	converged	converged	converged
$\dot{N} = 7.5 \cdot 10^{20}$ at/s		converged		
$\dot{N} = 8 \cdot 10^{20}$ at/s		rad. collapse	converged	converged
$\dot{N} = 1 \cdot 10^{21}$ at/s			converged ‡	converged
$\dot{N} = 1.3 \cdot 10^{21}$ at/s				rad. collapse

Table 1. Summary of the cases with prescribed power and seeding rate.

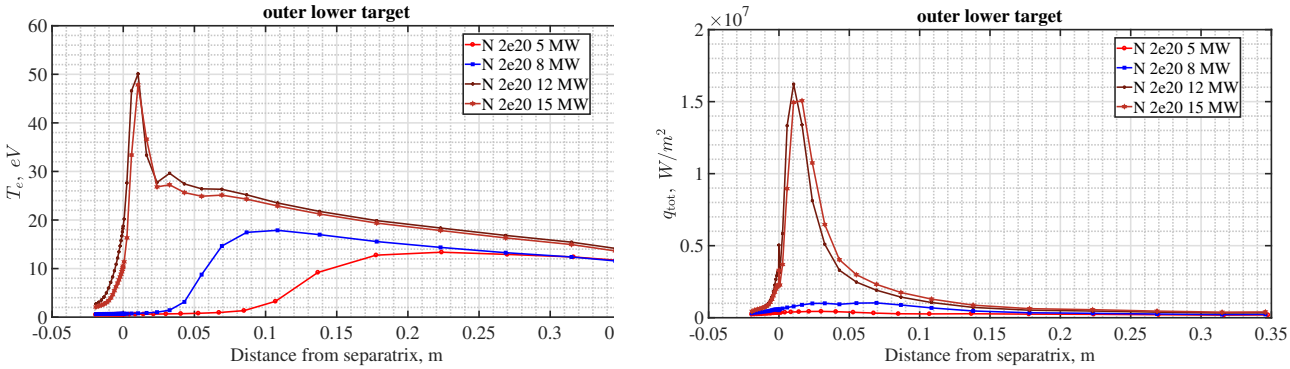

Figure 2. Electron temperature and heat flux density profiles along outer target for the cases with fixed seeding rate ($2 \cdot 10^{20}$ at/s) and varying discharge power.

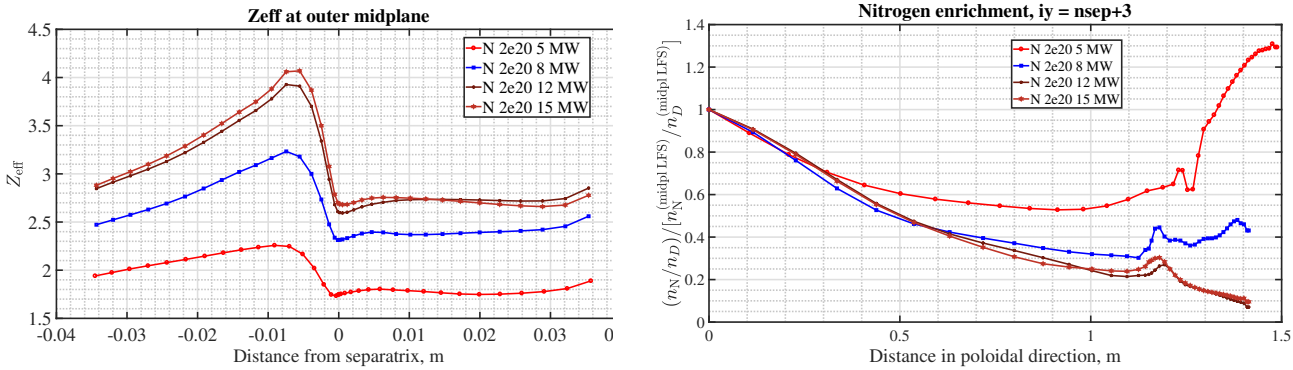

Figure 3. Z_{eff} at the outer midplane (OMP) and nitrogen enrichment along the flux surface located at 2 mm (as measured at OMP) from the OMP to outer target.

one can see that the closer the outer target is to detachment, the further the stagnation point of the nitrogen poloidal flow is from the target, and, consequently, the bigger the probability for nitrogen ions to return back to the target after recycling and re-ionization. Note also that, for the first two cases (which are closer to detachment), there is no impurity leakage from the high field side (HFS) at all, in contrast to the two attached cases. Consequently, the nitrogen upstream density increases with increasing discharge power.

The same tendency is illustrated by two dimensional plots of nitrogen density for all four cases, see Figure 5.

Now let's consider the series with maximal achievable seeding rate for various discharge power. Corresponding OMP and outer target profiles are presented in Figure 6. The four cases in this series

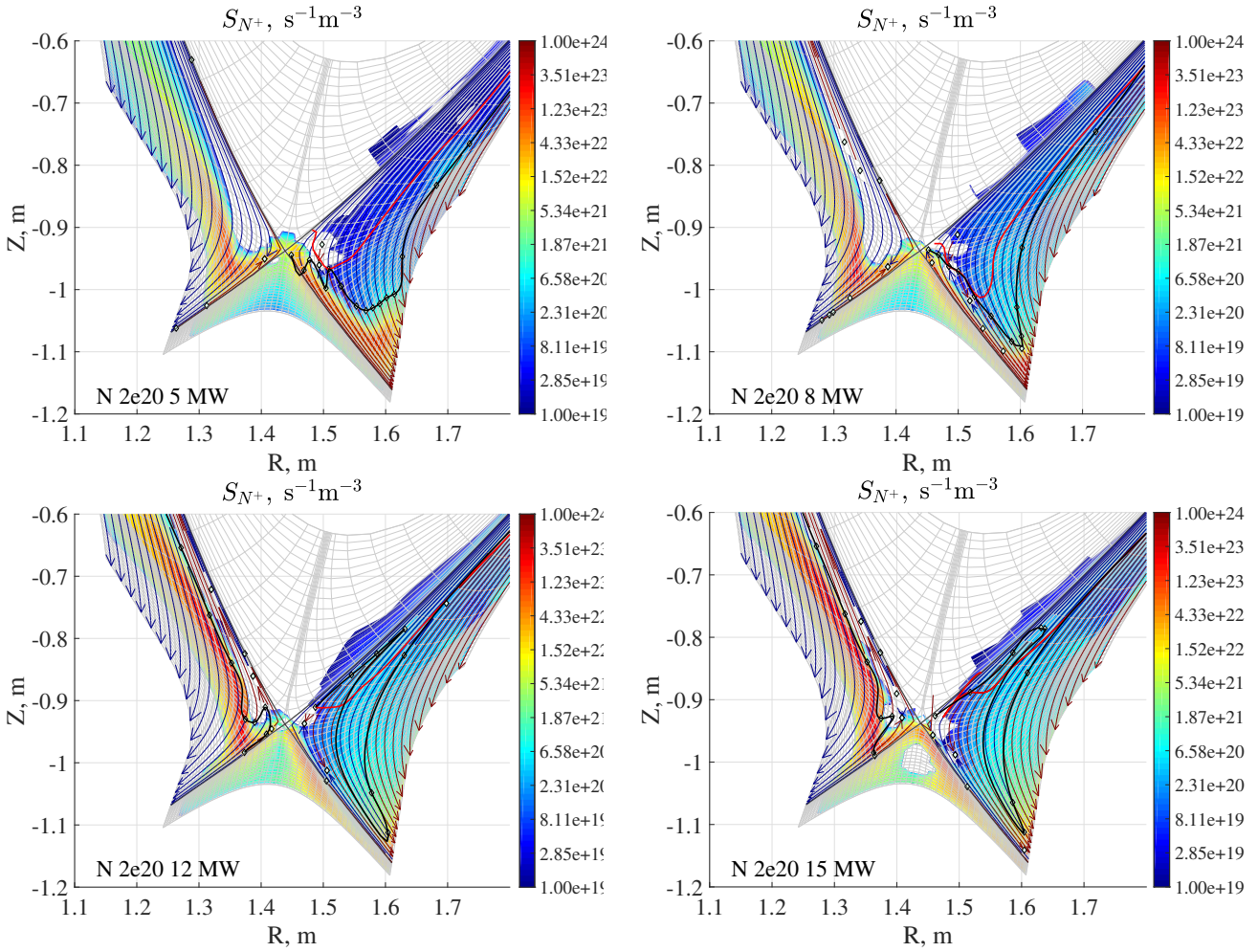

Figure 4. Nitrogen ionization source strength from neutral to first ionization state (contour plot) and the direction of net nitrogen ion *poloidal* flow (red and blue arrows). The colorbar indicates the ionization source strength. Red arrows correspond positive poloidal flux density (with regard to the direction of increasing poloidal coordinate x), blue arrows to negative poloidal flux density. White diamonds represent stagnation points, i.e. places where the poloidal flux is zero. Thus, each arrow connects either two stagnation points or a stagnation point and a target. Note that ends of arrows which are directed upstream are not seen in this figure, because corresponding stagnation points are located outside the plotted fragment of the computational domain. The thick red line is a spline interpolation of the stagnation points of the Deuterium poloidal flow (which is not presented in this Figure), while the black line does the same for nitrogen. If the spline is not plotted at the HFS, then the flow is directed towards the inner target throughout the visible part of the computational domain.

have similar conditions at the outer target – detachment everywhere along the target except in the far SOL wing, where the conditions correspond to the high-recycling regime. (Note that there were no aim to fit the seeding rate so that profiles at the outer target would be exactly the same). This is quite natural, since at higher power a larger amount of nitrogen is needed to radiate away this power.

The increasing discharge power leads to an increase of the electron temperature in the confined region, since the anomalous transport coefficients remain the same. Increasing the nitrogen seeding rate increases the nitrogen density and the effective charge. Note that with increasing nitrogen density, the deuterium density decreases.

It is worth mentioning that no significant decrease of the radial energy flux is observed near the separatrix on closed flux surfaces. This indicates that the amount of radiated power from the core is

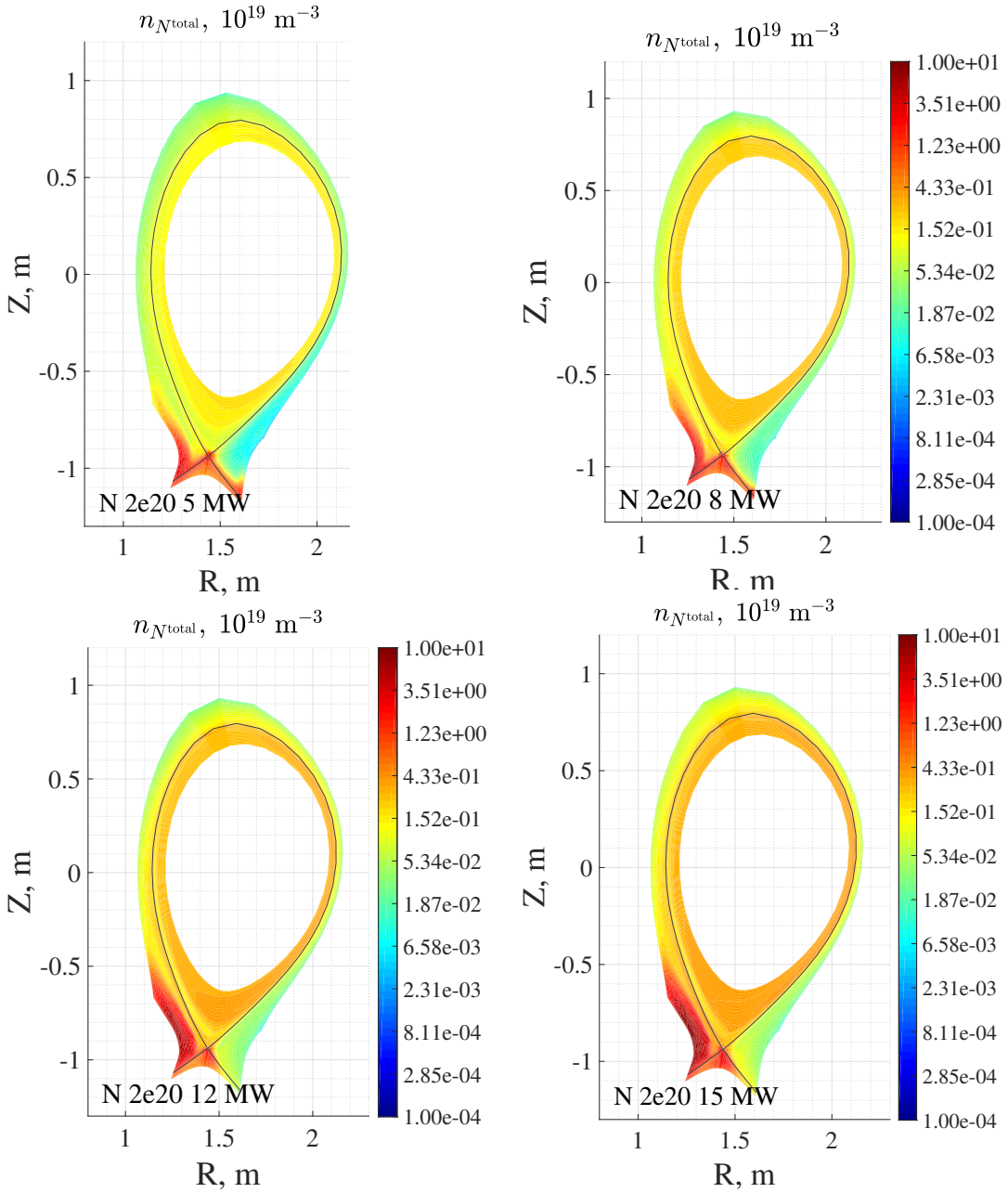

Figure 5. 2D distributions of nitrogen density for fixed seeding rate ($2 \cdot 10^{20}$ at/s) and varying discharge power.

small.

This is also seen from 2D plots presented in Figure 7 for one of the four cases considered – for other cases these profiles are quite similar. Here, one can see that most of the divertor region is cooled below 3 eV, however, no significant reduction of the electron temperature on the closed flux surfaces is obtained in the calculations. Most of the ionization during the recycling process takes place outside the separatrix, both for deuterium and for nitrogen. Figure 7 d) illustrates the nitrogen ion (summed over all ionized nitrogen states) and neutral fluxes in the divertor region and in the X-point vicinity. One can see that most nitrogen ions after ionization return back to the divertor targets, while only a tiny fraction of them contribute to the fluxes in the SOL above the X-point. This confirms the statement on the good nitrogen retention near the divertor targets.

Radiation losses, which give the major contribution to the electron power losses due to inelastic collisions, show only a tiny bright spot near the X-point, but this spot is located outside the separatrix

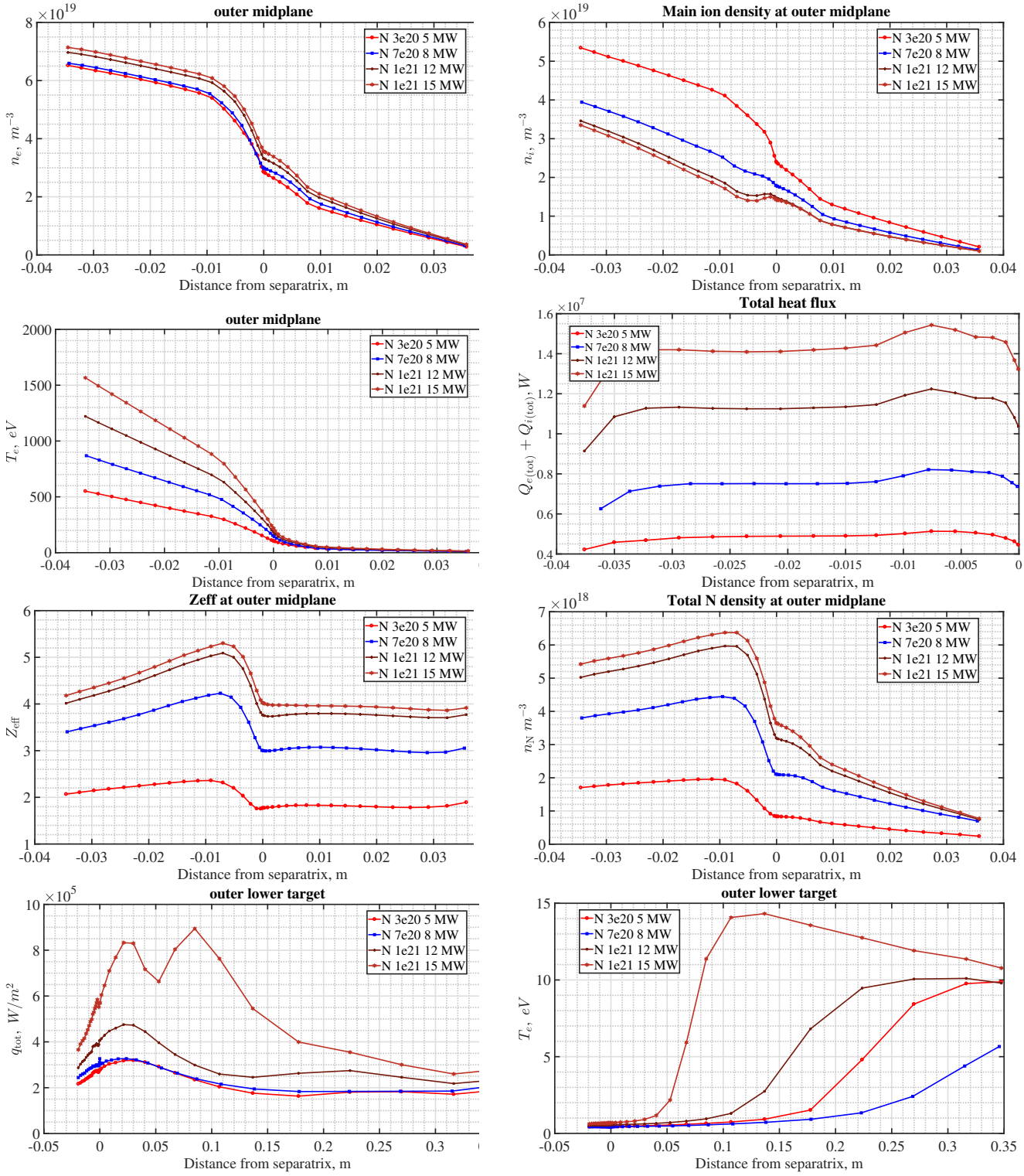

Figure 6. Outer midplane and outer target profiles for 4 cases with maximal achievable seeding rate for various discharge power.

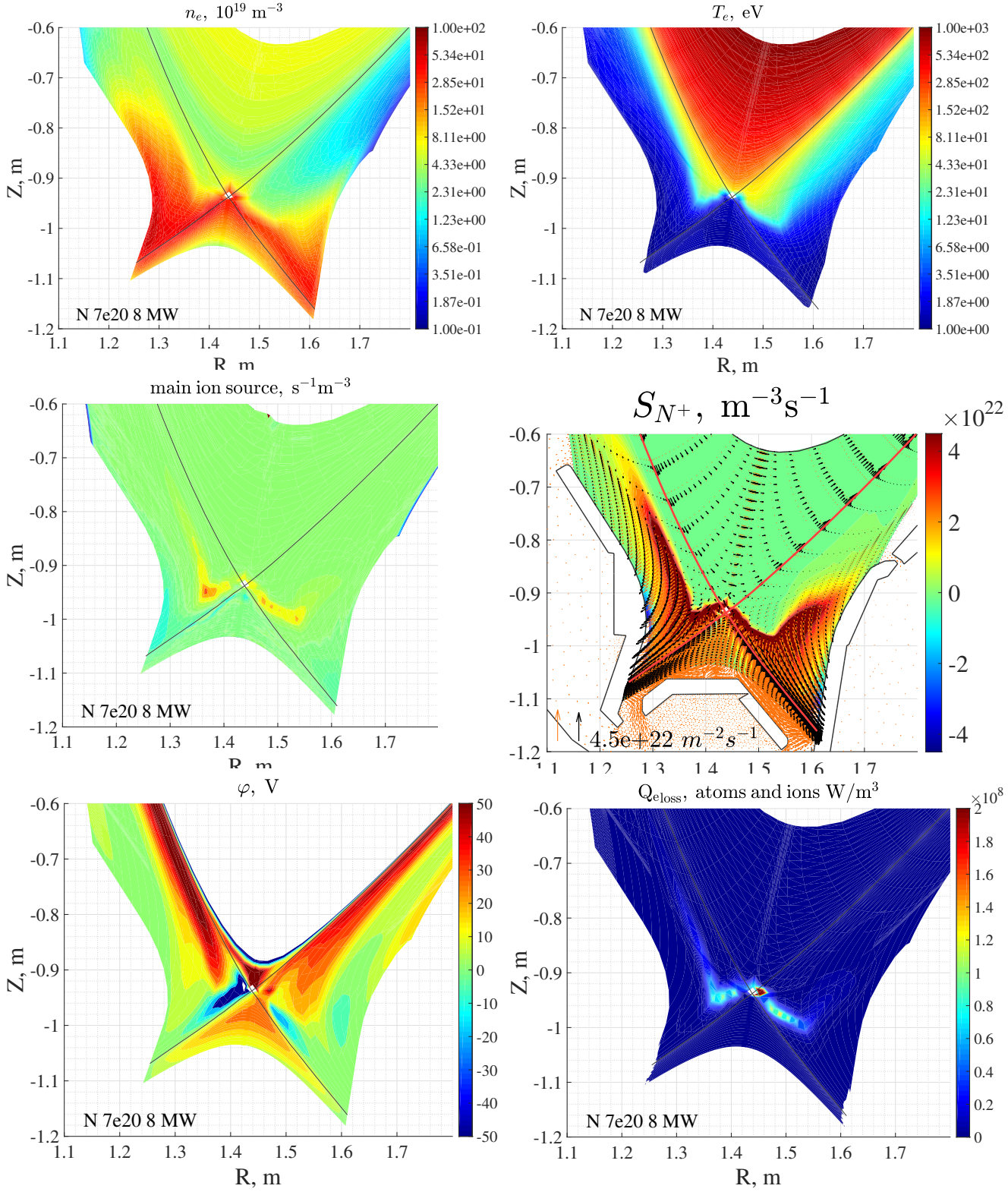

Figure 7. 2D profiles of electron density, electron temperature, ionization sources from neutral to first ionized state for deuterium and nitrogen, electric potential, and electron energy losses due to inelastic collisions for one of the cases with maximal achievable seeding rate. In the viewgraph d) (containing the nitrogen source) the colorbar corresponds to the source density, black arrows represent the nitrogen ion flux density (summed over all charged states) and orange arrows represent the nitrogen atoms flux density; corresponding scales for flux density vectors are given at the bottom.

rather than in the confined region 10 cm above.

Further increase of the nitrogen seeding rate leads to radiation collapse of the simulation.

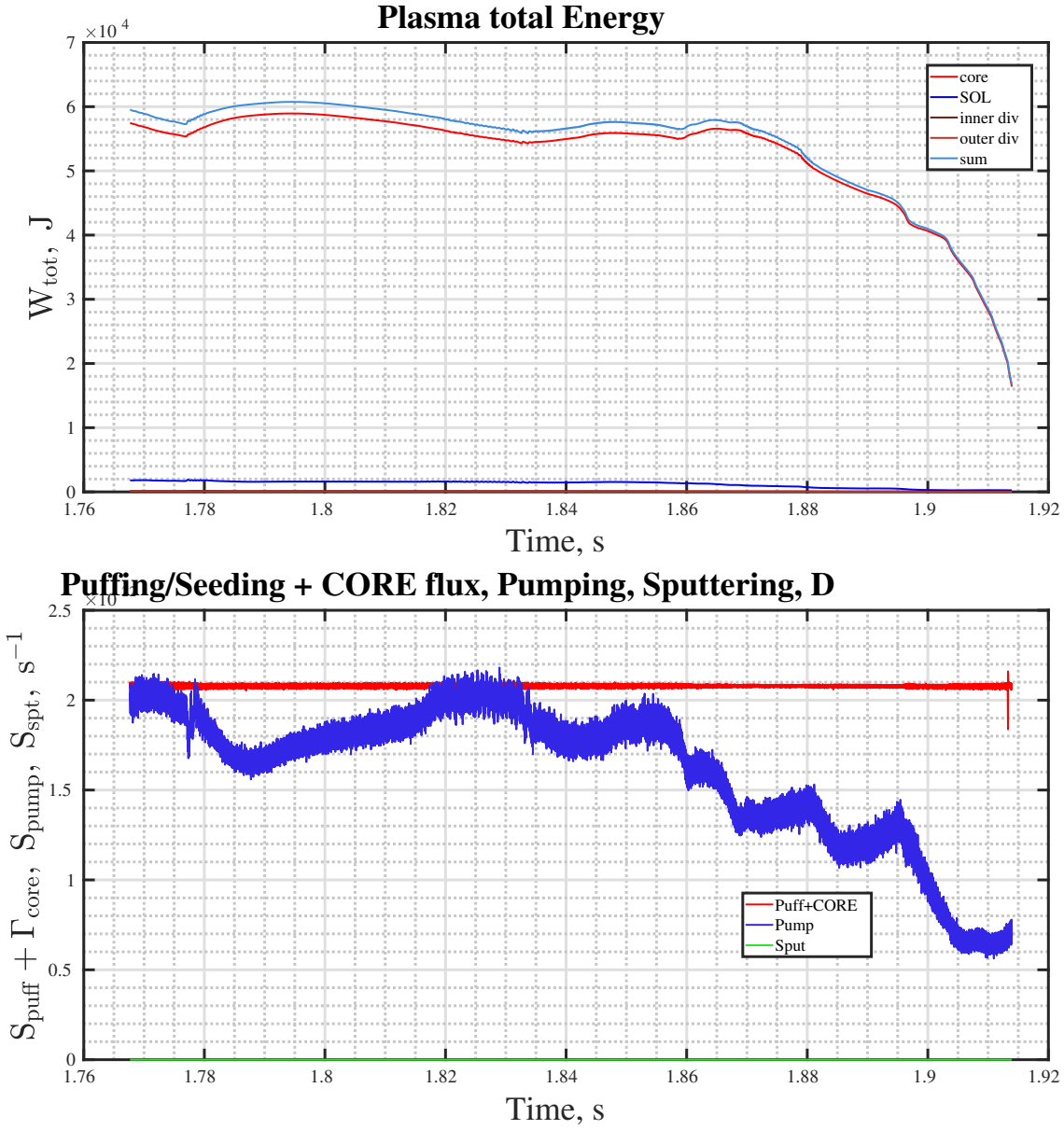

Figure 8. Time traces of total stored energy (in different regions) and of puffing and pumping rates of Deuterium for the case running into radiative collapse.

This may be illustrated by the time traces of such quantities like plasma total stored energy $\frac{3}{2}\int(n_eT_e+\sum_a n_aT_i)dV$ and puffing/pumping rates. Corresponding plots for the unstable case with 12 MW power and $1.4\cdot10^{21}$ nitrogen atoms/s are presented in Figure 8. One can see that the total energy content in the core decreases with time and simultaneously the number of pumped particles reduces for the main ions. For nitrogen, the pumping rate trace is not shown, but it is similar to the one for Deuterium. In a steady state solution, pumping compensates the puffing plus ion flux through the core, and, as the number of pumped particles reduces, the puffed particles go inside the confined region rather than to the pump. The radiation collapse appears because the incoming power is not sufficient to ionize all these particles and to compensate the radiation losses. Such a behavior is typical for cases where the nitrogen seeding rate exceeds the threshold value independently of the incoming power. The case with moderate seeding rate ($2\cdot10^{20}$ nitrogen atoms/s) and increased fueling rate (up to $3\cdot10^{22}$ deuterium atoms/s) behaves similarly.

Note that all the effort described above in Section 2 and in Appendix A leads to the increase of

the threshold value of the seeding rate from $2 \cdot 10^{20}$ atoms/s (as it was reported earlier in [28]) to $3 \cdot 10^{20}$ atoms/s for the 5 MW input power series, or helps to obtain a steady state solution for the case with seeding rate $1 \cdot 10^{21}$ atoms/s and 12 MW power, which earlier crashed due to numerical problems, but have not helped to avoid the radiation collapse: now the typical behavior of traces is seen for larger seeding rate values, and that is all.

Thus, the modeling scenario is suggested to be changed, and this is described in the next Section.

4. Cases with fixed particle content

Since the driving mechanism for the instability leading to the radiation collapse is found to be the imbalance between puffing and pumping rates both for deuterium and the impurity, it is suggested to change the strategy and fix the particle content in the system (i.e. in the computational domain) rather than fueling/seeding and pumping. This may be done by the reduction of fueling/seeding rate simultaneously with pumping rate by a factor of 1000, so that in these new scenarios the particle balance looks like a balance between particles coming from the core and particles removed out from the system by pumping. For deuterium, the typical flux from the core (representing the NBI) was $8 \cdot 10^{20}$ ions/s, so the reduction of the puffing from $2 \cdot 10^{22}$ to $2 \cdot 10^{19}$ atoms/s makes the fueling rate indeed negligible. The particle content is now controlled by the changing of the type of boundary conditions at the core boundary of the computational domain from the condition of prescribed particle flux to the condition of prescribed ion density. The value for this boundary condition is chosen to be $6.5 \cdot 10^{19}$ m^{-3} (which approximately corresponds to the stable solution of the 12 MW series with maximum achievable fueling rate), so that the resulting deuterium flux appears to be approximately unchanged (i.e. close to $8 \cdot 10^{20}$ ions/s).

The situation with nitrogen is similar: its seeding rate was reduced down to $1.4 \cdot 10^{18}$ atoms/s (which corresponds to the unstable case considered at the end of the previous section), and its content is varied by varying the density of the `N7+` ion at the core boundary in the range from $1.0 \cdot 10^{18}$ m^{-3} to $1.4 \cdot 10^{19}$ m^{-3}. For the rest of the nitrogen ionization states, the boundary conditions are set to require a zero gradient in the radial direction. The resulting nitrogen flux through the core boundary appears to vary from $5 \cdot 10^{19}$ to $2 \cdot 10^{20}$ ions/s, which is much bigger than the seeding rate in these modeling cases, but is still smaller than the total volume-integrated source of nitrogen ions due to ionization of nitrogen neutrals (without account of the nitrogen ion sink due to recombination either in the volume or on targets and walls) – $(0.8-1.2) \cdot 10^{22}$ s^{-1}. Consequently, the fact that the nitrogen comes into the system from the core rather than from the seeding valve seems to be not so dramatic.

In order to make sure that the power is enough to maintain the discharge with the parameters considered, the boundary conditions for the electron and ion temperatures are also changed from prescribing the power influx in the electron and ion channels to prescribing the temperature values themselves. The latter are chosen to be $T_e = T_i = 450$ eV.

The boundary values for density and temperature correspond to the intermediate plasma state of the case with 12 MW power and $1.4 \cdot 10^{21}$ at/s nitrogen seeding rate, which exhibit the desired radiating cold spot about 8 cm above the X-point before proceeding further to radiation collapse. This plasma state corresponds to the time of 1.888 s in the Figure 8. Thus, one might expect that starting from the desired plasma state, fixing the particle content and allowing the power to adjust to the actual radiation losses one gets the steady state solution with all desired features. The cases with smaller nitrogen content represent then the experimental conditions when the seeding rate is reduced by the feedback loop. They are summarized in Table 2. Note that in this series the discharge power is computed, and not prescribed.

$n_{\mathrm{D+}}^{(core)}$	$n_{\mathrm{N7+}}^{(core)}$	$T_e^{(core)}$	$T_i^{(core)}$	P
$5 \cdot 10^{19}$ m^{-3}	$1 \cdot 10^{18}$ m^{-3}	450 eV	450 eV	3.4 MW
$5 \cdot 10^{19}$ m^{-3}	$2 \cdot 10^{18}$ m^{-3}	450 eV	450 eV	4.0 MW
$5 \cdot 10^{19}$ m^{-3}	$3 \cdot 10^{18}$ m^{-3}	450 eV	450 eV	4.6 MW
$5 \cdot 10^{19}$ m^{-3}	$4 \cdot 10^{18}$ m^{-3}	450 eV	450 eV	5.3 MW
$5 \cdot 10^{19}$ m^{-3}	$5 \cdot 10^{18}$ m^{-3}	450 eV	450 eV	6.0 MW
$5 \cdot 10^{19}$ m^{-3}	$6 \cdot 10^{18}$ m^{-3}	450 eV	450 eV	6.8 MW
$5 \cdot 10^{19}$ m^{-3}	$7 \cdot 10^{18}$ m^{-3}	450 eV	450 eV	8.3 MW
$6.5 \cdot 10^{19}$ m^{-3}	$8 \cdot 10^{18}$ m^{-3}	450 eV	450 eV	15.5 MW
$6.5 \cdot 10^{19}$ m^{-3}	$1.0 \cdot 10^{19}$ m^{-3}	450 eV	450 eV	14.7 MW
$6.5 \cdot 10^{19}$ m^{-3}	$1.2 \cdot 10^{19}$ m^{-3}	450 eV	450 eV	16.1 MW

Table 2. Summary of the cases with fixed particle content.

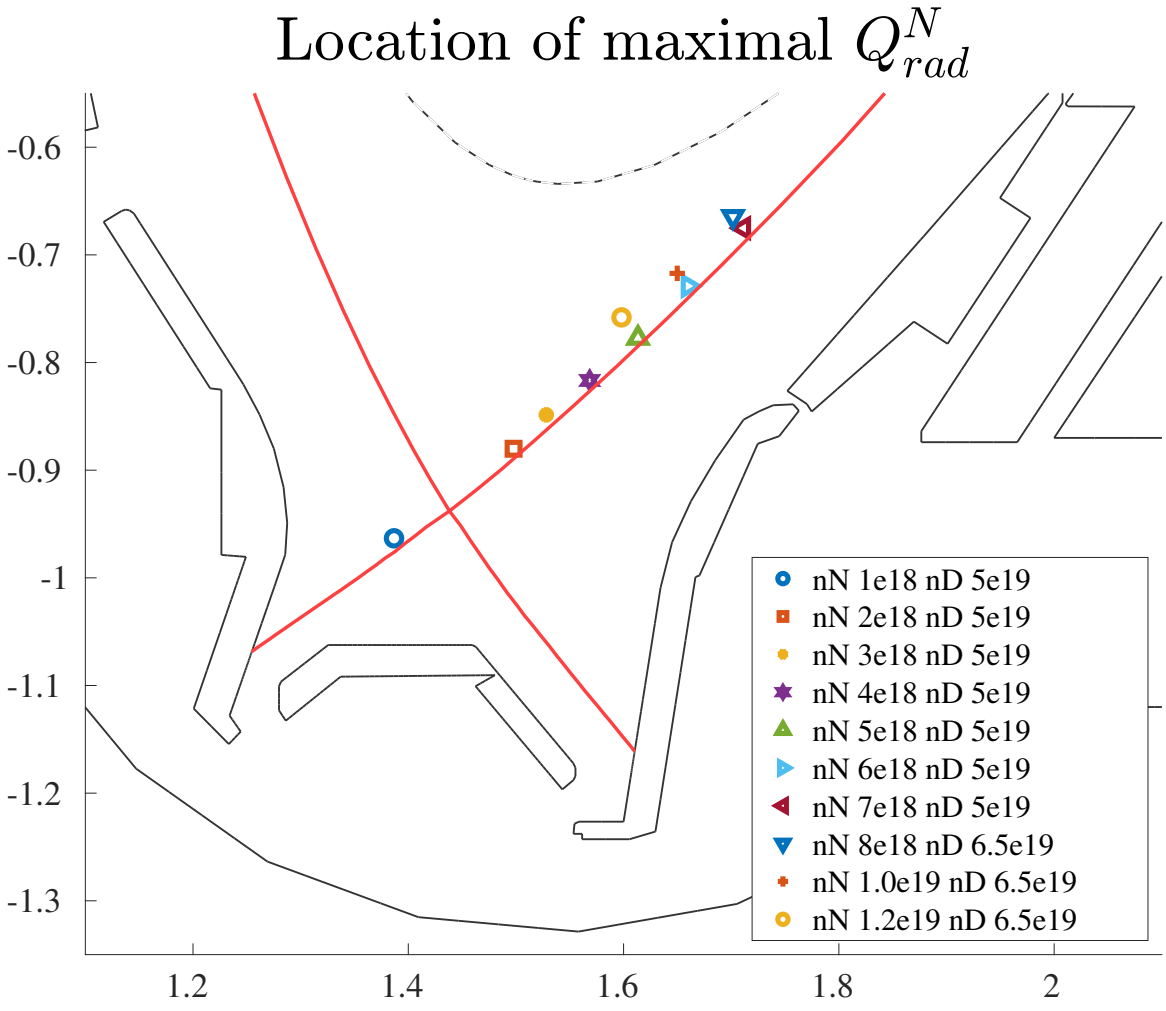

Figure 9. Locations of the maximum of nitrogen radiation density for the cases listed in Table 2.

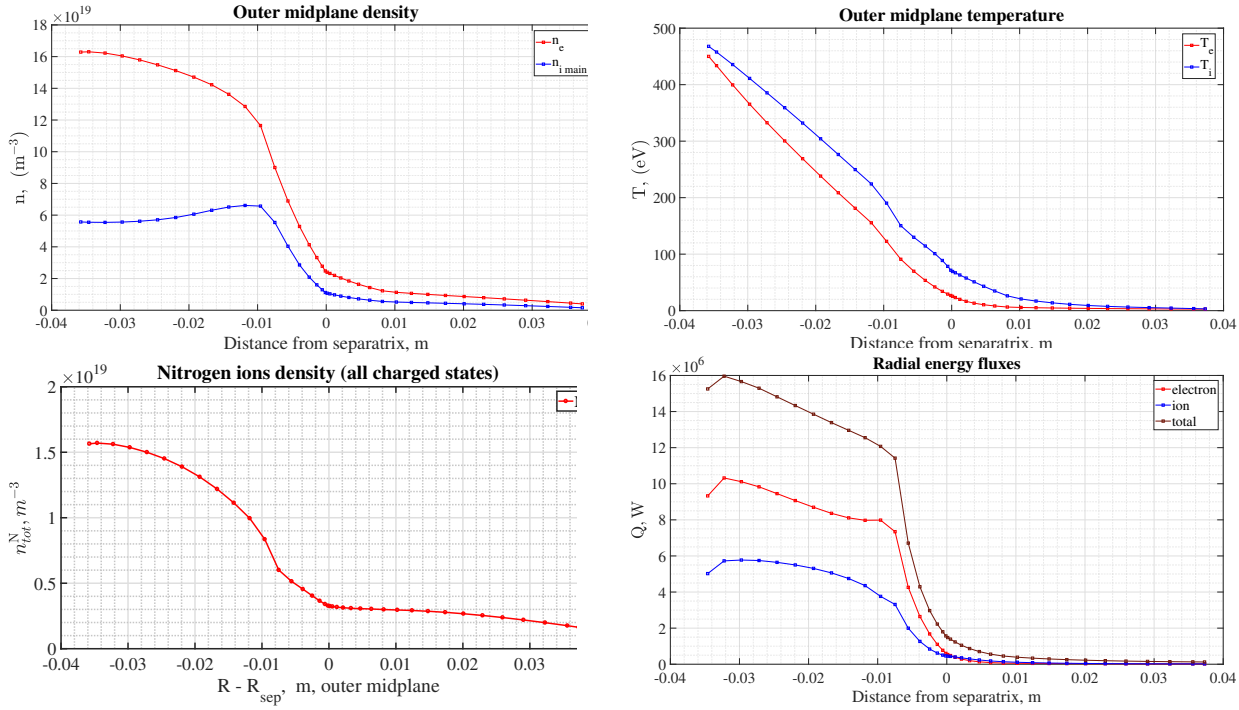

Figure 10. OMP profiles of electron, ion, nitrogen density, electron and ion temperatures, and total energy flux through closed magnetic flux surface for the stable case with maximal nitrogen content.

With increasing nitrogen density, the location of the radiation loss maximum moves from the inner SOL (case with attached outer target, first line in Table 2) towards the OMP along the separatrix (see Figure 9), and then shifts back down and simultaneously inside the confined region. An attempt to increase the nitrogen content further and to see whether the radiating spot would appear exactly above the X-point leads to the radiation collapse.

Thus, in the series of runs considered, the stable case with the largest possible nitrogen content corresponds to that with `N7+` boundary density $1.2 \cdot 10^{19}\ m^{-3}$. The computation results for this last stable case are presented and discussed below.

The corresponding electron, main ion, and nitrogen ion densities, ion and electron temperatures, and energy flux across the flux surface inside the separatrix as functions of the radial distance from the separatrix measured at the OMP are presented in the Figure 10. The main features are that the incoming power of about 15 MW is spent almost entirely in the confined region, and only 2 MW crosses the separatrix, while the OMP separatrix temperature remains relatively high to make plasma still fully ionized.

The 2D profiles of the main plasma parameters are presented in Figure 11. In comparison to Fig 7, one can see that the maximum of the radiation density profile is indeed located in the confined region about 15 cm above the X-point, but it is shifted to the low field side (LFS). In fact, there is a poloidally narrow radiating band with a rotated bow-like shape, which touches the separatrix about 25-30 cm above the X-point at both HFS and LFS, and is maximally away from the separatrix exactly above the X-point, at about 14 cm. Comparing the electron power loss density profile to the temperature profile, one can see that the electron temperature in this band is about 10-15 eV. This corresponds to the temperature of the nitrogen cooling rate maximum [38] and to the fact that most of the electron energy losses occur through nitrogen radiation – calculation shows that the total power dissipated by nitrogen radiation is about 13 MW for this case. Note that ions also spend their energy through the exchange with electrons, while electrons directly excite the nitrogen ions.

In the whole zone below this radiating band (and above the separatrix), the electron temperature

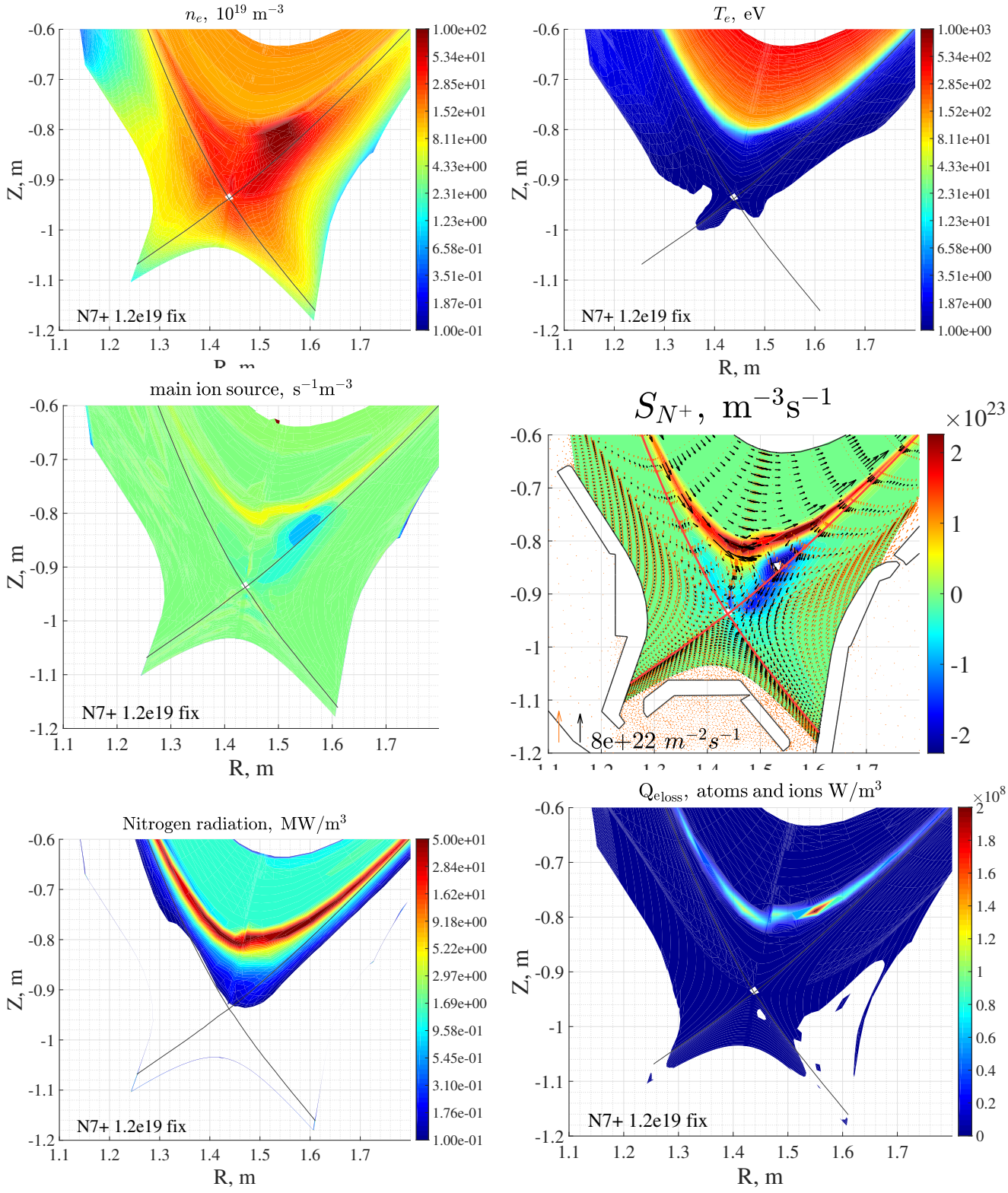

Figure 11. 2D profiles of electron density, electron temperature, ionization sources from neutral to first ionized state for deuterium and nitrogen, nitrogen radiation, and electron energy losses due to inelastic collisions for the case with maximal fixed nitrogen content. The meaning of the colorbars and arrows is the same as in Fig 7.

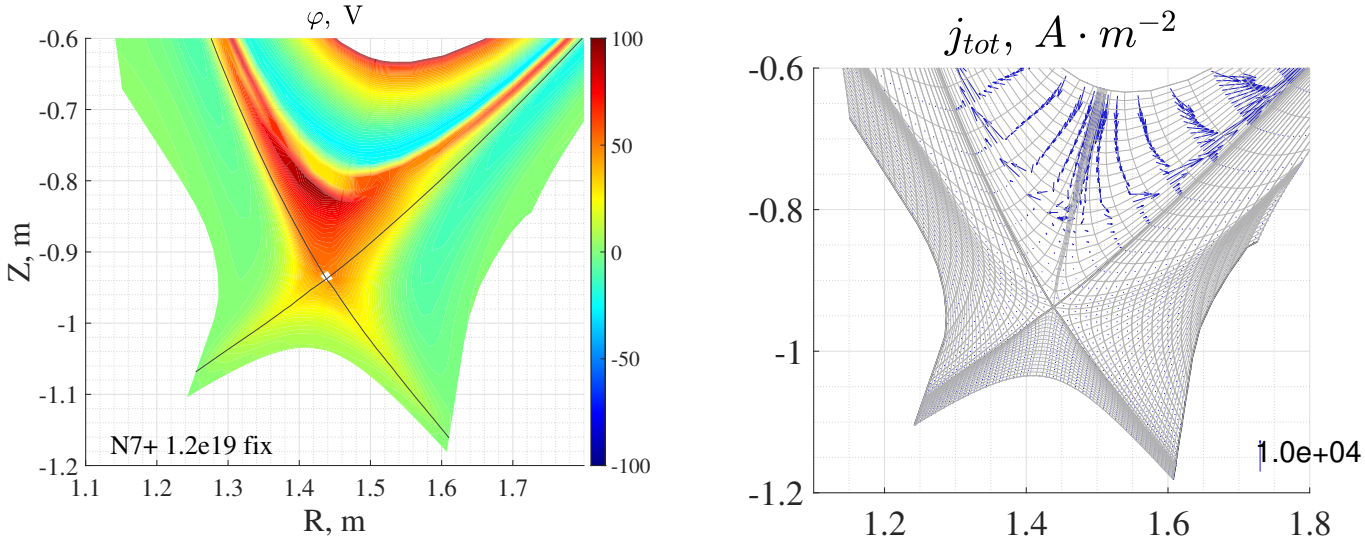

Figure 12. 2D profiles of electric potential and current density for the case with maximal fixed nitrogen content.

is very low - about 2 eV or even lower, so that volumetric recombination is possible and takes place inside the separatrix. This is seen in the corresponding 2D plot.

Thus a strong poloidally localized perturbation of all plasma parameters appears in the regime with strongly radiating X-point. The vertical size of this perturbation is $14-16$ cm if it is measured above the X-point in vertical direction. If this size is mapped to the OMP along the flux surfaces, then the corresponding distance in horizontal direction is about $7-8$ mm, which is seen in Fig 10 as a starting point of discharge power decay. Note that the corresponding effective flux expansion factor (which is defined as the ratio of vertical size of perturbation measured above the X-point to the horizontal size of perturbation measured at the OMP) reaches the value of 20 here. Thus the perturbation remains within the transport barrier, which is set up to be 9 mm wide (at the OMP) through the prescribed profiles of anomalous transport coefficients, which are exactly the same for all series of runs. This means that no effect of radiaiting X-point formation on the transport barrier (its position, width, strength etc) is considered, since anomalous transport coeficients profiles are the input data for SOLPS-ITER simulaiton.

From the 2D temperature profile one can see that the whole region below the X-point is colder than 1 eV – almost no power enters the divertor region, and both divertors are in full detachment.

The very important feature of the regime with radiating X-point is the appearance of the strong peak in the electrostatic potential profile above the X-point in the confined region, see Figure 12. This peak corresponds to the strong poloidal electric field, which is required to drive the Pfirsch-Schlüter current through the cold plasma of low electrical conductivity. This Pfirsch-Schlüter current is necessary, as usual, to close the current caused by vertical drift of guiding centers in the inhomogeneous B-field – the corresponding electric current flow pattern is shown in Fig 12. Note that the ratio $e\varphi/T_e > 50$ at the location of the potential maximum, and is about $10-20$ in the PFR, thus causing strong $E \times B$ drift fluxes. This mechanism of potential peak formation is similar to the one discussed in [31, 32]. A side remark is that if the toroidal B-field has the opposite direction, both the ∇B-induced current and the Pfirsch-Schlüter current would change their direction too, as well as the poloidal electric field. Thus a potential minimum and not a maximum would appear – the effect would be exactly the same as the X-point potential minimum formation in the conventional regime with unfavorable toroidal magnetic field direction, discussed in detail in [33].

The consequence of the potential maximum is a vortex $E \times B$ drift, which may be seen in

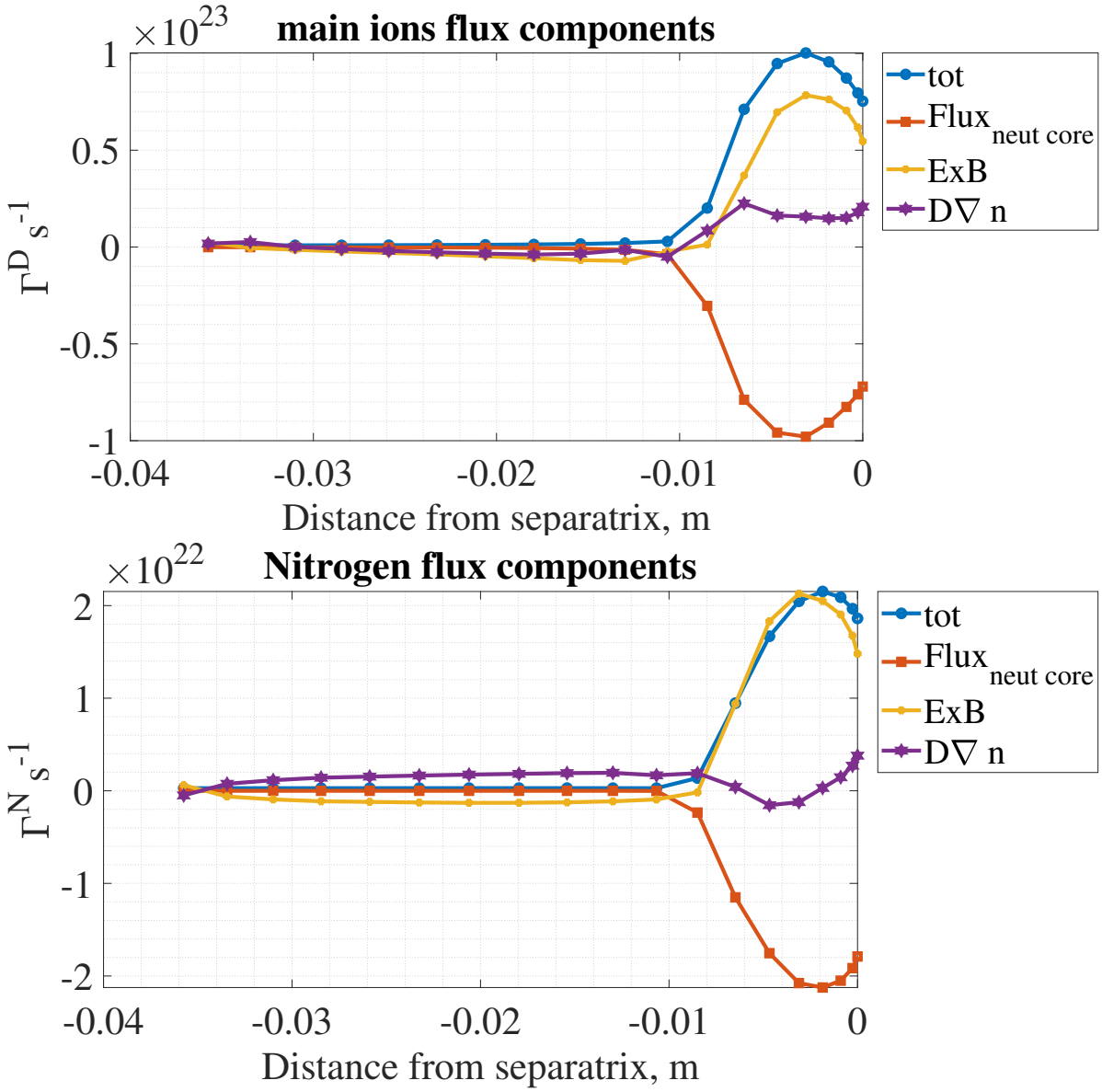

Figure 13. Deuterium and nitrogen radial fluxes, integrated over magnetic flux surfaces. Shown are total ion flux (for nitrogen – summed over all ionized charge states), contributions from anomalous diffusion and from $E \times B$-drift, and neutral flux (negative, because it is directed inwards)

Figure 11 d), and this $E \times B$ drift flow appears to give the major contribution to the main ion and impurity fluxes in the vicinity of the X-point. The last statement is illustrated in Figures 13 and 14. One can see that in the zone perturbed by the cold X-point, the $E \times B$ drift drags nitrogen ions away from the confined region, and the main contribution to the poloidally integrated $E \times B$ drift flow comes from the cold zone in the X-point vicinity, and the same is true for main ions.

As a result, the impurity flow pattern changes significantly with respect to the attached and/or semi-detached regimes. In the regime with cold X-point, impurities are born due to ionization inside the separatrix, about 10 cm above the X-point. Since it is the zone of strong E-field, they are immediately dragged away by the vortex drift flow. Some fraction of them recombine inside the separatrix (behind the radiating band, where the temperature is low), others either cross the separatrix at the LFS, or flow above the X-point and cross the separatrix at the HFS. The latter ions continue their vortex motion and return back to the confined region a little bit further upstream, but some fraction of them go further in the SOL and then flow to the inner target. The nitrogen ion flux from the core to the SOL at the LFS then splits into two fluxes. The frst is directed towards

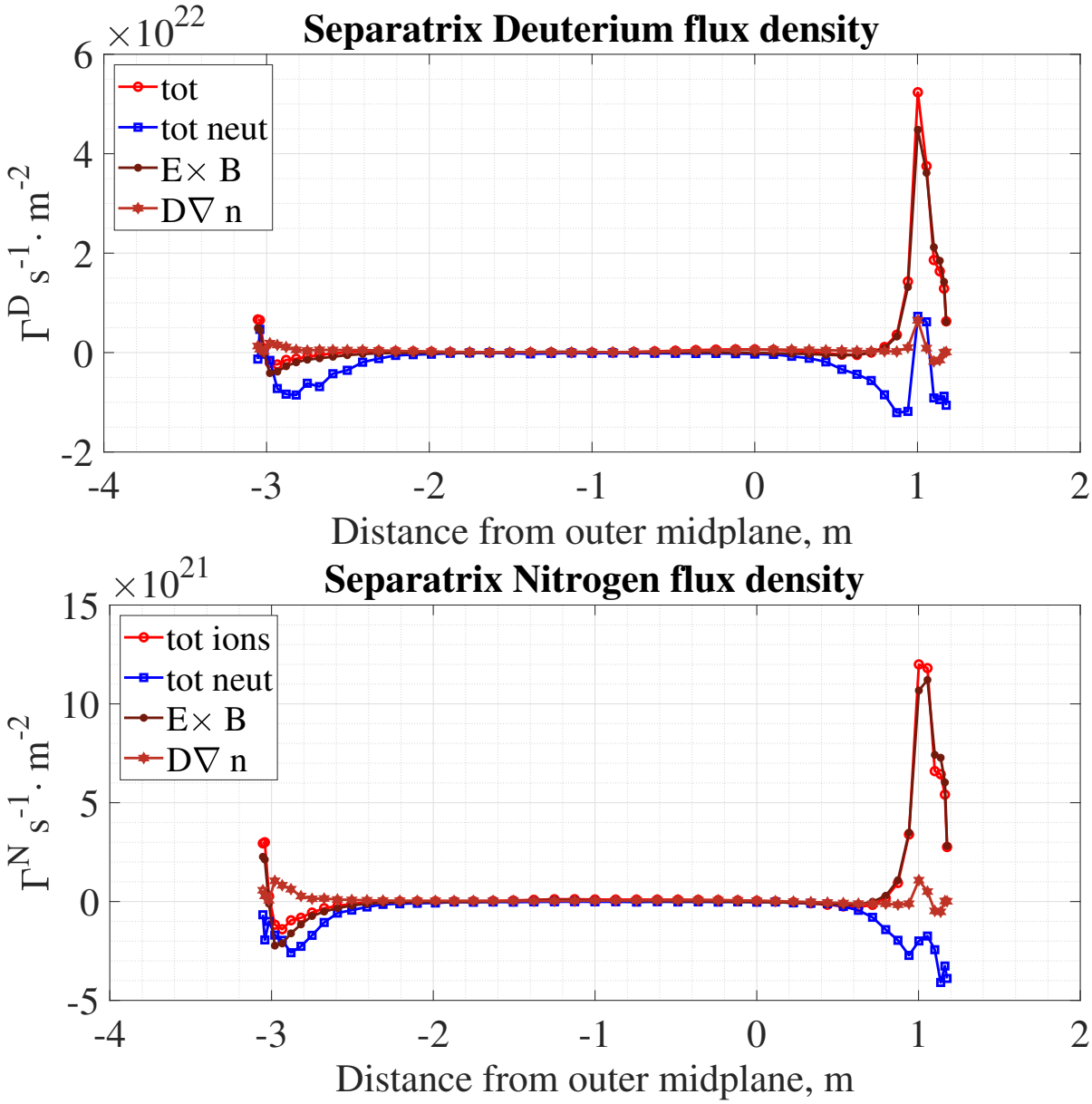

Figure 14. Deuterium and nitrogen radial fluxes density across the separatrix. Shown are total ion flux (for nitrogen – summed over all ionized charge states), contributions from anomalous diffusion and from $E \times B$-drift, and neutral flux (negative, because it is directed inwards)

upstream, and returns to the inner divertor through the OMP, the top of the machine and the inner midplane. The second one turns towards the outer divertor, however, most of these particles either recombine in the volume or turn to the PFR dragged by the $E \times B$ drift flow. Thus only a small part of the ions are able to reach the outer target. Those ions which turn into the PFR continue their flow towards the SOL at the HFS, however, their flux decays due to volumetric recombination. Finally, only a small amount of ions crosses the separatrix at the HFS and turn towards the outer target, where they join the parallel flow coming from the inner midplane. And again, both these flows decay in the SOL at the HFS due to volumetric recombination, and again the flux reaching the inner target appears to be very small. Finally, the recombination decay of the nitrogen ion flux is compensated by the neutral return fluxes, which are directed from the divertor region to the radiating spot above the X-point, where the ionization takes place.

The plasma profile inhomogeneity on closed flux surfaces is illustrated in Figure 16, where the computed electron temperature and main ion parallel velocity are plotted for each flux surface

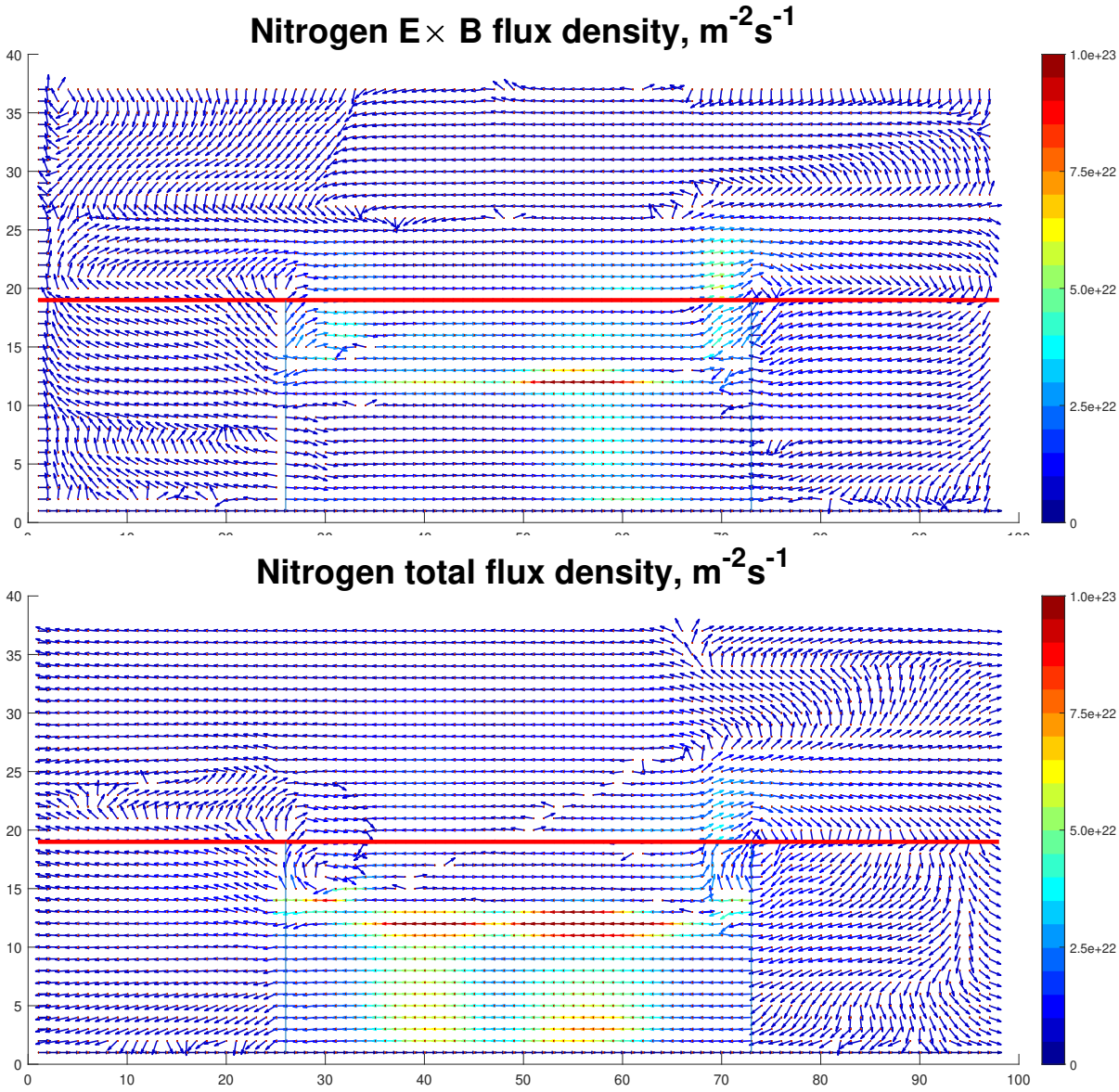

Figure 15. $E \times B$ and total nitrogen flux density on B2.5 computational mesh. Numbers along axes are cell numbers, which are used as poloidal (x) and radial (y) coordinates. Inner and outer targets are located at the left and right boundaries of the computational domain correspondingly. The red line represents the separatrix, the SOL is located above the red line. The two thin blue lines represent the topological cuts, which separate the HFS and LFS parts of the PFR (located to the left and to the right correspondingly) and the confined region (CORE, which is located in between). Cuts are fully non-transparent for fluxes, e.g. a flux which reaches the left cut from the PFR side (from the left) continues at the right side of the right cut (again in the PFR), and a flux which reaches the left cut from the CORE side (from the right) continues at the left side of the right cut (again in the CORE) – i.e. periodic boundary conditions are assumed at cuts. All arrows have the same length, the magnitude of flux density is represented by color.

over the computational mesh versus the poloidal distance. One can distinguish so-called regular inner surfaces with almost constant electron temperature and regular cosine-like parallel velocity and perturbed outer ones, where temperature goes down in the X-point vicinity and velocity deviates from what might be expected from a neoclassical solution. Such a behaviour is explained by the presence of heat sinks and particle sources (due to ionization and recombination), but the details of the momentum transport analysis for such a situation are beyond the scope of this paper and are left for future work.

Such a parallel velocity perturbation affects significantly the radial electric field, see Figure 17. One can see that, on the perturbed flux surfaces (the 8 outermost ones), the radial electric field shear changes sign, and the electric field itself appears to be positive. Such a perturbation not only changes the poloidal $E \times B$ drift flow direction, but also might affect the turbulence suppression and confinement mode. Note that those latter effects cannot be modelled by SOLPS-ITER because it lacks a turbulent transport model suitable for the edge plasma.

5. Description of the regime with radiating spot above the X-point

To understand what happens in the radiating X-point regime, let's start from mentioning that such a cold zone above the X-point behaves as an energy sink, while the energy comes from the core across the flux surfaces (see Fig. 18). In this sense, the radiating X-point behaves like a divertor in a conventional high-recycling regime, where the radial energy flux crosses the separatrix and turns into parallel conductive energy flux. To estimate the characteristic perpendicular energy flux decay length λ_q, one may say that the divergence of the perpendicular anomalous heat flux is equal to the divergence of the parallel conductive heat flux:

$$\frac{1}{\lambda_q}\chi_e^{(AN)} n_u \frac{T_u}{\lambda_q} \approx \frac{1}{L_\parallel}\frac{T_u}{m_e \nu_{ei}} n \frac{T_u}{L_\parallel},$$

where index u stands for upstream and $L_\parallel$ is the distance, along the magnetic field line, from upstream to the point where the electron temperature becomes negligibly small. Thus $L_\parallel$ may be estimated as qR, and one gets the following expression for λ_q:

$$\lambda_q = qR\sqrt{\frac{m_e \nu_{ei} \chi_e^{(AN)}}{T_u}} \tag{1}$$

Exactly the same estimates are valid for the energy flux decay length $L_\perp$ in the radiating X-point regime: again it is assumed that the cross-field flux comes mainly at the OMP and then turns into parallel conductivity flux which ends above the X-point, and the parallel connection length may be again estimated as qR.

For ASDEX Upgrade, this estimate gives $L_\perp \approx 2.3$ mm for $T_u = 120$ eV, $\chi_e^{(AN)} = 0.6\ m^2/s$, and $n_e = 8 \cdot 10^{19}\ m^{-3}$. This value agrees reasonably well with the energy flux profile presented in Figure **??**.

As the energy flux travels downstream along the magnetic field, the temperature decreases, and reaches T_r – the temperature of maximal impurity cooling rate, which for nitrogen may be roughly estimates as $T_r = 12$ eV. At or near this point all energy flowing from upstream is dissipated by impurity radiation, and the energy balance looks like

$$\frac{B_{pol}}{B h_x}\frac{\mathrm{dq}_\parallel}{\mathrm{dx}} = -n_e n_N R_N(n_e, T_e) \tag{2}$$

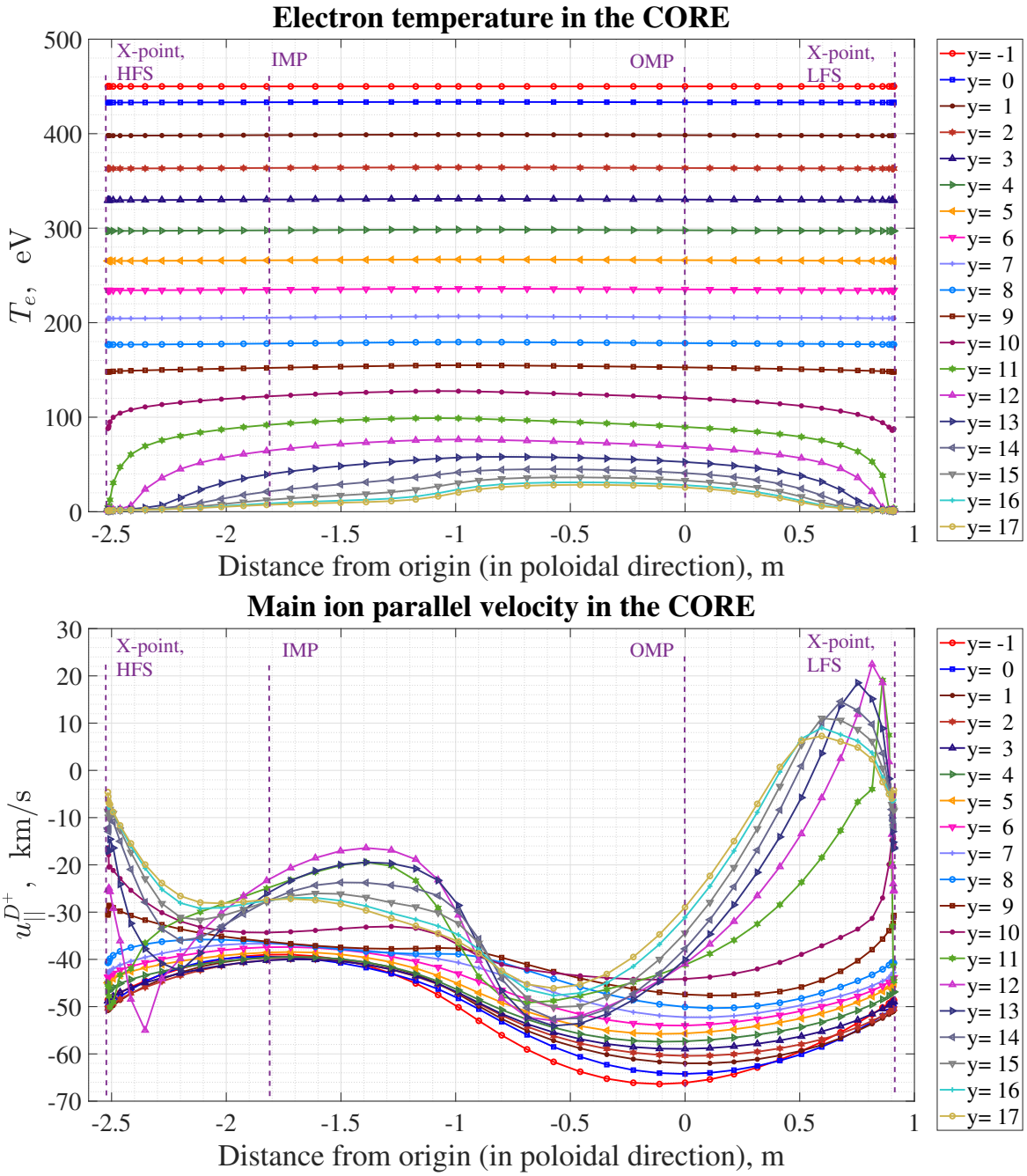

Figure 16. Electron temperature and Deuterium parallel velocity along all 19 closed flux surfaces versus poloidal distance measured along the core boundary, y is the flux surface label, $y = -1$ corresponds to the core boundary of computational domain, $y = 17$ corresponds to the separatrix.)

where n_e is the electron density, n_N is the nitrogen density (summed over all ions plus neutrals), and $R_N(n_e, T_e)$ is the impurity cooling rate, h_x is a metric coefficient. Let's roughly estimate the poloidal size L_{pol} of the intensive radiation zone, assuming that there is almost no radiation upstream (due to the higher temperature and lesser density of both electrons and nitrogen) and there is no radiation beyond the radiation zone (because all energy has already been radiated away), and the divertors are power-starved.

Integrating Eq. (2) along the poloidal direction x from x to $x + L_{pol}$, one gets:

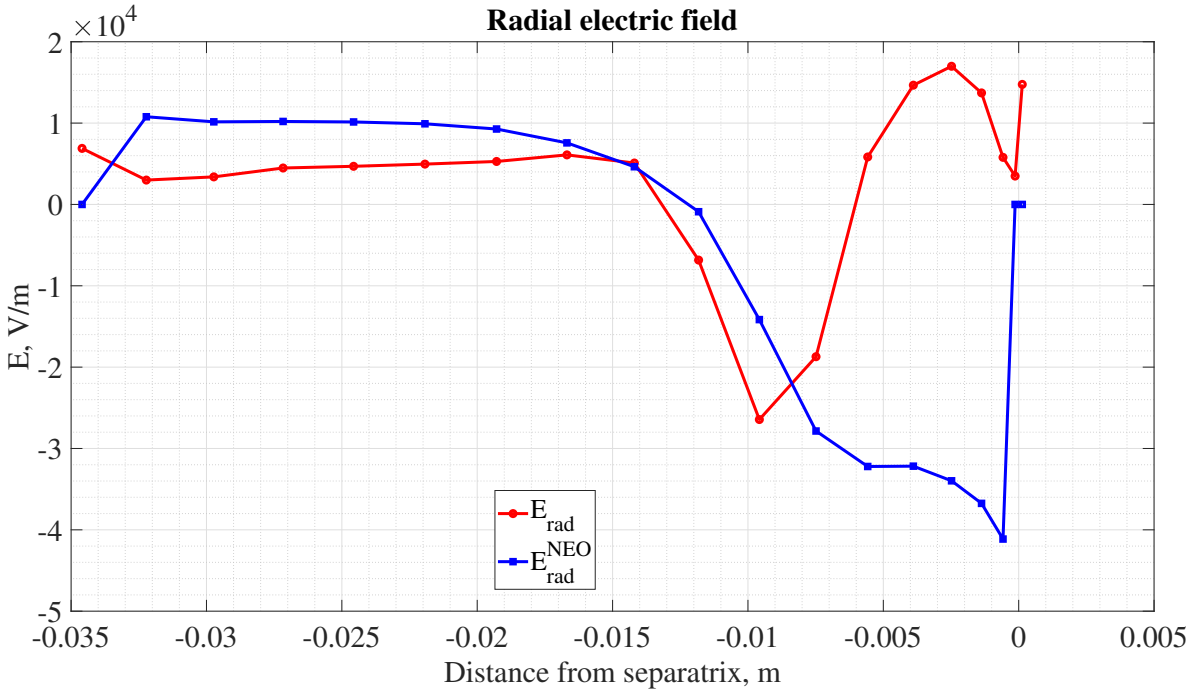

Figure 17. Computed and neoclassical radial electric fields, calculated based on the OMP ion temperature, density, and velocity radial profiles.

$$q_{\parallel}\big|_{x}^{x+L_{pol}} = -\int_{x}^{x+L_{pol}} \frac{B n_e n_N R_N(n_e,T_e) h_x}{B_{pol}} \mathrm{dx} \tag{3}$$

The parallel energy flux at the entrance to the radiating zone (at x) may be roughly estimated as $q_{\parallel} \sim \dfrac{T_u^{7/2} k_0}{L_{\parallel}}$ with $k_0 = \dfrac{n_e}{m_e \nu_{ei} T_e^{3/2}} = \dfrac{3(4\pi\varepsilon_0)^2}{4\sqrt{2\pi m_e} e^4 \Lambda} = 4.95 \cdot 10^{68}$ SI units, $\Lambda \approx 12$ is the Coulomb logarithm, while the energy flux behind the radiating zone may be treated as zero. Roughly estimating the integral in the left hand side of Equation (3) as $L_{pol} n_e^{(max)} n_N^{(max)} R_N^{(max)}$, assuming that maximal radiation corresponds to the maximum of the impurity cooling rate, one gets for the poloidal size of the radiaiting band (see Fig. 18):

$$L_{pol} = \frac{T_u^{7/2} k_0 B_{pol}}{L_{\parallel} n_e^{(max)} n_N^{(max)} R_N^{(max)} B}. \tag{4}$$

For $T_u = 120$ eV, $L_{\parallel} = qR = 5{\cdot}1.65\ m$ and $B/B_{pol} \approx 10$ for AUG, $n_e^{max} = 10^{21}\ m^{-3}$, $n_e^{max} = 10^{20}\ m^{-3}$, $R_N^{(max)} = 8 \cdot 10^{-32}\ m^3/s$ one gets $L_{pol} \approx 2.4$ cm.

As it is mentioned above, there is no radiation behind this band, because no power reaches this zone to provide ionization and radiaton. The temperature here is about 1 eV, volumetric recombination overcomes electron impact ionization, and neutrals can freely move in this zone. Ionization naturally takes place at or near the radiating band, because the temperature here is already high enough for ionization, and there is enough power. Above the radiating band (towards upstream), the radiation is not so intensive since both electron and impurity densities decrease and the nitrogen cooling rate decreases two orders of magnitude as the electron temperature increases from 12 eV up to about 100 eV [38].

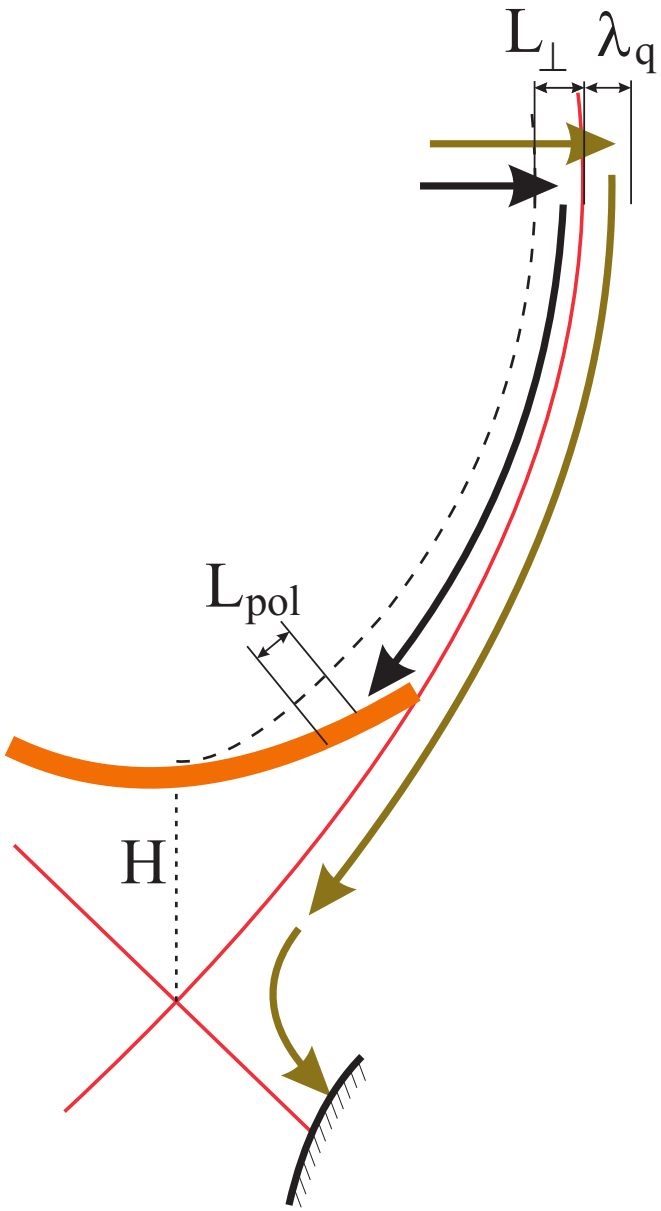

Figure 18. Schematic picture of the heat flow in the core in the presence of a radiative X-point. The orange thick line represents a radiating band, H denotes the height of the radiating spot above the X-point. The dark green line shows the heat flow in the SOL in the high-recycling divertor operation regime.

6. Conclusions

An ASDEX Upgrade H-mode discharge with extreme nitrogen seeding rate is modelled by means of the SOLPS-ITER plasma edge transport code. The seeding rate is large enough to fully detach the outer target and even push the discharge into a regime with a radiating spot above the X-point, which was recently observed in the experiment.

Attempts to simply increase the seeding rate in the modeling lead to unstable cases, which go into radiative collapse if a certain threshold in seeding rate is exceeded. This threshold value increases with discharge power, however, a larger power influx appears not to be helpful in avoiding the radiation collapse. Considering the cases with fixed seeding rate and varying the discharge power, the conclusion is derived that the larger the power, the better the nitrogen leaks from the targets. In other words, the better the degree of detachment is (no matter how it is exactly defined), the better

the nitrogen is compressed near the divertor targets.

To achieve regimes with a radiating spot above the X-point, it appears to be necessary to prescribe particle content in the system rather than fueling/seeding and pumping rates, by applying boundary conditions of another type. This represents experimental conditions where the particle content is controlled by varying the seeding rate in real time in a feedback loop. Thus the stable solution is obtained with up to 90% of discharge power radiated away from inside the separatrix.

Features of such a regime are analyzed. It is demonstrated that in a such regime both targets are in full detachment, since very little power crosses the separatrix. The characteristic radial power decay width on closed flux surfaces is estimated to be of the same order as λ_q in the conventional regime, since the radiating spot acts as the heat sink like the divertor does for the energy flux crossing the separatrix.

The poloidal size of the radiating spot is estimated to be of the order of 2 cm for ASDEX Upgrade parameters. Since all available energy is radiated away from this spot, no energy goes beyond it, and a zone of cold plasma ($T_e \approx 1$ eV) appears inside the separatrix above the X-point. Since the vertical ∇B current still enters this cold zone from the top, it should be closed by Pfirsch-Schlüter currents, and, to drive these Pfirsch-Schlüter currents through this cold highly resistive plasma zone, a strong electric field is required. Consequently, a peak of electrostatic potential appears in the cold zone above the X-point, leading to large $E \times B$ drift flows of main ions and impurity. These drift flows give the major contribution to the net particle flows, thus changing the impurity flow pattern completely in comparison to the semi-detached regime.

Strong poloidal inhomogeneity of the plasma profiles on closed flux surfaces cooled by intensive radiation together with the presence of intensive ionization sources there change the parallel velocity with respect to its neoclassical profile. Consequently, the radial E field deviates from the neoclassical one, which might improve the turbulence suppression.

Acknowledgments

This work was performed at the Peter the Great Saint Petersburg Polytechnic University with support from the Russian Foundation for Basic Research, Grant No. 20-52-53025. Numerical calculations were performed at the Polytechnic SuperComputer Center at Peter the Great St. Petersburg Polytechnic University. Authors thank Dr Felix Reimold for his help in preparing the input data for the simulations. The views and opinions expressed herein do not necessarily reflect those of the ITER Organization.

Appendix A. Model improvements to avoid radiation collapse

In this Appendix we describe some attempts to improve the simulation model as compared to [28] in order to avoid the radiation collapse.

Appendix A.1. Turning off the speed-up scheme of artificial poloidal averaging

A very natural first step is to turn off the so-called speed-up scheme of partial flux surface averaging [37], or at least to suppress it for those poloidal rings near the separatrix which are expected to be perturbed by the radiating spot above the X-point. Indeed, this speed-up scheme suppresses the formation of main ion density poloidal variations on the flux surfaces, and therefore cannot be applied for flux surfaces with an existing cold zone above the X-point. The price for it is having to decrease the time step and the necessity to wait much longer for the runs to converge.

Appendix A.2. Turning on the flux-limiting factor inside the separatrix

The second step is turning on the flux-limiting options for the conductive electron and ion heat fluxes along the magnetic field on the closed flux surfaces. Due to the notable difference in electron and ion temperatures between upstream and the cold X-point region, the heat flux densities towards the cold spot are expected to be of the same order as in the SOL, where they are known to be kinetically limited, so that the flux limit in the core should be introduced in the same manner as it is done outside the separatrix – see details in [34].

Appendix A.3. Playing with mesh resolution near the X-point

The third step is playing with the computational mesh resolution in both poloidal and radial directions near the X-point, where the computational cell shape is not strictly rectangular, and numerical effects are expected to be maximal.

In fact, all meshes have the same number of cells in all regions, the same position of the separatrix and cuts, but different size of mesh cells (different values of metric coefficients h_x and h_y) near the X-point. Note that increasing the mesh resolution near the X-point in the radial direction leads to a coarser grid in the far SOL (since the position of the far SOL boundary of the computational domain and number of mesh cells remain unchanged), and the same is true in the poloidal direction. Also it is worth noting that playing with mesh resolution does not necessarily improve the orthogonality of the mesh and does not necessarily reduce the mesh distortion.

Appendix A.4. Changing the numerical approximation of the drift terms

Consequently, an attempt is made to improve the numerical approximation of the drift terms to make sure that e.g. $\left(\nabla \cdot \left[\vec{\mathbf{E}} \times \vec{\mathbf{B}}\right] / B^2\right)$ and $\left(\nabla \cdot \left[\nabla p \times \vec{\mathbf{B}}\right] / B^2\right)$ are numerically zero in a spatially constant B field even for non-orthogonal and/or distorted meshes. Another requirement is that radial components of the $E \times B$ drift and diamagnetic drift fluxes vanish numerically if the electrostatic potential and pressure correspondingly are poloidally constant. These conditions might be important near the X-point, where the drift flux gives the major contribution to the total flux. This requires the product BR (vacuum B field times major radius) to be numerically constant independently of whether it is computed at cell centers, cell faces, or cell corners, and it is necessary that the poloidal flux between neighbouring flux surfaces is conserved. Since the latter are geometrical properties of the mesh, the preprocessing routines which compute geometrical quantities and metric coefficients have been improved accordingly to enforce these properties.

All the features described above are implemented and available in the latest version (3.0.7) of the SOLPS-ITER code suite.

References

[1] R.A. Pitts *et al* 2011 *Journal of Nuclear Materials* **415** S957–S964
[2] R.A. Pitts *et al* 2019 *Nuclear Materials and Energy* **20** 100696
[3] M. Wischmeier *et al* 2015 *Journal of Nuclear Materials* **463** 22–29
[4] R.P. Wenninger *et al* 2014 *Nucl. Fusion* **54** 114003
[5] H. Zohm *et al* 2013 *Nucl. Fusion* **53** 073019
[6] G. Zhuang *et al* 2019 *Nucl. Fusion* **59** 112010
[7] A. Loarte *et al* 2011 *Physics of Plasmas* **18** 056105
[8] S. Potzel *et al* 2014 *Nucl. Fusion* **54** 013001
[9] F. Reimold *et al* 2015 *Nucl. Fusion* **55** 033004

[10] A. Kallenbach *et al* 2015 *Nucl. Fusion* **55** 053026
[11] H. Meyer, for the AUG Team *et al* 2019 *Nucl. Fusion* **59** 112014
[12] A.R. Field *et al* 2017 *Plasma Phys. Control. Fusion* **59** 095003
[13] C Guillemaut *et al* 2017 *Plasma Phys. Control. Fusion* **59** 045001
[14] S. Glöggler *et al* 2019 *Nucl. Fusion* **59** 126031
[15] M.L. Reinke *et al* 2011 *Journal of Nuclear Materials* **415** S340–S344
[16] J. A. Goetz *et al* 1999 *Physics of Plasmas* **6** 1899
[17] D. Eldon *et al* 2019 *Nuclear Materials and Energy* **18** 285-290
[18] T.W. Petrie *et al* 2007 *Journal of Nuclear Materials* **363-365** 416-420
[19] M. Bernert *et al* 2017 *Nuclear Materials and Energy* **12** 111-118
[20] F. Hitzler *et al* 2020 *Plasma Phys. Control. Fusion* **62** 085013
[21] M. Bernert *et al* 2019 3rd IAEA Technical Meeting on Divertor Concepts, 4-7 November 2019, Vienna, Austria, `https://conferences.iaea.org/event/192/` (Link may be replaced if new publication appears during the reviewing procedure)
[22] M. Barbarino *et al* 2020 *Nucl. Fusion* **60** 097001
[23] B. Lipschultz *et al* 1984 *Nucl. Fusion* **24** 977
[24] M.Z.Tokar 2002 *Physics of Plasmas* **96** 1646
[25] P.B. Snyder *et al* 2019 *Nucl. Fusion* **59** 086017
[26] F. Reimold *et al* 2015 *Journal of Nuclear Materials* **463** 128–134
[27] F. Reimold *et al* 2017 *Nuclear Materials and Energy* **12** 193-199
[28] I. Senichenkov *et al* 2019 *Plasma Phys. Control. Fusion* **61** 045013
[29] S. Wiesen *et al* 2015 *Journal of Nuclear Materials* **463** 480-484
[30] X. Bonnin *et al* 2016 *Plasma and Fusion Research* **11** 1403102
[31] V. Rozhansky *et al* 2018 *Contrib. Plasma Phys.* **58** 540-546.
[32] A.E. Jaervinen *et al* 2017 *Nuclear Materials and Energy* **12** 1136–1140
[33] M. Wensing *et al* 2020 *Nucl. Fusion* **60** 054005
[34] V. Rozhansky *et al* 2009 *Nucl. Fusion* **49** 0250007
[35] D. Reiter. The EIRENE Code User Manual. Available at http://www.eirene.de
[36] R. Schneider *et al* 2006 *Contrib. Plasma Phys.* **46** 3–191
[37] E. Kaveeva *et al* 2018 *Nucl. Fusion* **58** 126018
[38] T. Pütterich *et al* 2015. Proceedings of 42^{nd} EPS conference on Plasma Physics. ECA Vol. **39E** P4.111